Bioelectrochemistry 128 (2019) 165–174

Contents lists available at ScienceDirect

Bioelectrochemistry

journal homepage: www.elsevier.com/locate/bioelechem

Nanostructured Au-Pt hybrid disk electrodes for enhanced parathyroid hormone detection in human serum

Ajay Kumar Yagati [a,b], Anna Go [a], Sachin Ganpat Chavan [a], Changyoon Baek [a], Min-Ho Lee [a,*], Junhong Min [a,*]

[a] School of Integrative Engineering, Chung-Ang University, Heukseok-dong, Dongjak-gu, 06974 Seoul, Republic of Korea
[b] Institute of Analytical Chemistry/Chemo-and Biosensors, University of Regensburg, Universitätsstraße 31, 93053 Regensburg, Germany

ARTICLE INFO

Article history:
Received 1 February 2019
Received in revised form 9 April 2019
Accepted 9 April 2019
Available online 12 April 2019

Keywords:
Parathyroid hormone
Nanostructures
Disk electrode
Antibody
Impedance
Immunosensor
EIS
DPV

ABSTRACT

Most clinical tests for biomarker detection require the support of a laboratory, and the results are usually slow, less sensitive, and lack the possibility for Point-of-Care (PoC) testing. Further, with the increasing demand for sensitive, portable, rapid, and low-cost devices for clinical PoC applications, innovative methods are crucial. Thus, we report on utilizing nanostructured gold-platinum (Au-Pt) hybrid electrodes as a PoC device for highly sensitive and selective PTH detection in human serum samples. The method employs the immobilization of 3-mercaptopropionic acid to Au and subsequent activation of the carboxyl groups to enable anti-PTH antibody immobilization. Serum PTH was detected by monitoring the changes in electrochemical properties (ΔR_{ct} and Δi) of the sensor using electrochemical impedance spectroscopy (EIS) and differential pulse voltammetry (DPV) against a standard hexacyanoferrate (II/III) probe. Changes in relative response percentage (RR%) in electrochemical properties due to increased PTH concentrations in serum were observed with EIS and DPV. The biosensor exhibited a low detection limit of 0.36 pg.mL^{-1} (EIS) and 0.59 pg.mL^{-1} (DPV) in serum with a linear range of 1 to 100,000 pg.mL^{-1}. Further, to validate the accuracy of the proposed method, clinical samples ($n = 20$) were examined using the EIS method and compared to an established commercial test.

1. Introduction

Point-of-care (POC) testing has gained increasing popularity to replace laboratory testing due to its potential for faster therapeutic intervention, portability, and improved patient outcome [1–3]. Despite their convenience, existing PoC tests often cannot compete with the accuracy of a clinical lab, which is why there is still a need for development and improvement of sensitive PoC devices for improved patient outcomes in a cost-effective way [4–6]. Medical biosensors for point-of-care (POC) applications have gained tremendous advancement towards patient diagnosis and care because of their ability to reduce costs and, provide on the spot diagnosis. Thus, for sensitive determination of biomarker levels in the human body it is essential to develop simple, sensitive and economically feasible POC testing systems [7,8]. Enzyme-linked immunosorbent assay (ELISA) is the gold standard method commonly used for antigen-antibody reactions for clinical protein biomarker detection [9]. This approach is simple and accurate but has suffered from its inability of multiplexing, long analysis time, large sample volume and difficulty of interpretation between serotypes since low levels of antibodies are often undetectable or can exhibit cross-reactivity to different antigens. Also, liquid chromatography-mass spectrometry (LC-MS) based biomarker detection is highly selective and sensitive, easy to use, and allows multiplexing with adequate sensitivity [10]. However, its high cost, long assay times and technical sophistication make routine clinical diagnostics less feasible for PoC applications. Further, there are several commercially available biomarker analyzers for multiplexed detection based on surface plasmon resonance [11] (Horiba Inc., BIO-RAD), fluorescence [12] (Luminex, Myriad RBM), or electrochemiluminescence [13] (Roche Diagnostics). However, these commercial instruments are not appropriate for PoC applications in limited resource settings as they require expensive consumables including sample well plates, chips, and reagent kits [14]. Moreover, fluorescence-based detection strategies, on the other hand, require precise adjustment of laser and optical components. Thus, there is a quest for simple and cost-effective devices for multiple protein biomarker detections that could be employed in limited resource settings. Therefore, PoC, miniaturized and highly efficient ways to quantify biomarkers are crucial to control and prevent disease.

Electrochemical detection methods have attracted considerable interest because of their sensitivity, low cost, and inherent miniaturization. One of the key advantages of electrochemical biosensors relies on their relative simplicity. Inexpensive electrodes can be easily integrated with simple electronics to perform rapid measurements in miniaturized easy-to-use portable systems [15–17]. Considering these advantages of electrochemical biosensors, we focused on developing a sensitive and

* Corresponding authors.
E-mail addresses: mhlee7@cau.ac.kr (M.-H. Lee), junmin@cau.ac.kr (J. Min).

https://doi.org/10.1016/j.bioelechem.2019.04.011
1567-5394/

low-cost biosensor device for PoC applications to provide on the spot disease diagnostics for patient care systems. Further, electrochemical analysis using microelectrodes provides a vast number of fascinating characteristics due to their small electroactive area, smaller ohmic drop, low interfacial impedance and fast mass transfer due to radial diffusion at the electrode surface [18]. The overall surface area is modified to obtain better limits of detection, higher signal/noise (S/N) ratio and a wide dynamic range [19]. However, a weak output signal from the analyte limits the use of these microelectrodes to a specific range of analyte detections. Thus, methods in modifying the electrode platforms that result in enhanced analytical capability for cancer diagnostics are highly desired [20].

Nanostructured electrodes offer high surface areas and were often found to be the best performing transducer elements for electrochemical biosensors [21]. Among many materials for nanostructured electrodes, gold (Au) has emerged as a potential candidate due to its high electrical conductivity, mechanical stability, tunability and reusability [22]. Having better biocompatibility for immobilization and creation of a microenvironment for biomaterials to retain their activities with high stability and its easy accessibility to various surface chemistry procedures for bioconjugations Au nanostructured electrodes were extensively used as transducer interface for various designs of electrochemical sensors [23,24]. Despite many previous reports on the development of Au nanostructured electrodes as a biosensing element, there is still an ongoing search for better technologies to enhance the sensitivity of the transducer interface and decrease the analyte detection limit [25]. Recently, a method of thermal dealloying metal substrates to produce controlled nanostructure morphologies [26] was introduced. The resulting electrodes showed high electrical conductivity, large specific surface area, and exhibited a 10-fold increase in electrochemical current for DNA detection. Also, a 3D Au nanostructure with a large specific area [27] and superior conductivity [28] for enzyme-induced signal amplification [29] and electrodeposition procedures to form gold electrode substrates for an aptamer-based biosensor [30] were adopted. Recently, a sulfur-doped graphene matrix was reported [31] that enhanced electrocatalytic performance and also aptamer tri-infinite amplification labels for the detection of metalloproteinases-2 detection was reported [32]. We have also developed nanostructured electrochemical immunosensors featuring reduced graphene oxide and gold nanoparticle electrodes [18] for the detection of various protein biomarkers [33]. However, direct detection of Parathyroid hormone (PTH) in complex fluids using electrochemical impedance spectroscopy (EIS) [34] and differential pulse voltammetry (DPV) [35] has not been reported yet.

In this paper, we introduced a chemical solution phase route to produce nanostructured surfaces on platinum (Pt) disk electrodes as an electrochemical transducer for the detection of PTH biomarkers in a small blood sample. (Fig. 1a). Au structures on Pt disk electrodes were utilized to further enhance the bio-affinity reaction of PTH in complex samples (Fig. 1b). An optical image showing the sensing area of the proposed electrode is presented in Fig. 1c. PTH is a polypeptide with 84 amino acid residues that regulates the Ca^{2+} and HPO_4^{2-} levels and, its concentration in blood ranges between 10 and — 65 pg.mL^{-1} in healthy humans. Enhanced PTH levels are found in patients with hyperparathyroidism which results in numerous symptoms, including osteoporosis, cancer, heart, and autoimmune diseases. PTH acts as an early stage indicator for parathyroid cancer, which emphasizes the need for a sensitive and selective assay for early detection of PTH. A schematic illustration of the binding and detection of PTH in human serum is shown in Fig. 1d.

2. Experimental methods

2.1. Materials and reagents

Gold(III) chloride trihydrate ($HAuCl_4.3H_2O$; ≥99.9%), ammonium hydroxide (NH_4OH), sodium borohydride ($NaBH_4$), hydroxylamine (NH_2OH), N-(3-dimethylaminopropyl)-N′ ethyl carbodiimide hydrochloride (EDC, purum, ≥ 98.0%), N-hydroxysuccinimide (NHS, 98.0%), 3-mercaptopropionic acid (MPA, ≥99.0%), potassium hexacyanoferrate (III) ($K_3[Fe(CN)_6]$) and potassium hexacyanoferrate(II) trihydrate ($K_4[Fe(CN)_6].3H_2O$) were purchased from Sigma Aldrich. Monoclonal parathyroid hormone antibody (anti-PTH, 10–1579), parathyroid hormone antigen (PTH, 30R-2670) and thyroid-stimulating hormone (TSH) were obtained from Fitzgerald (MA. USA). Triiodothyronine (T_3, Human) was purchased from CalBioreagents (CA, USA), Human serum albumin (A9511), bovine serum albumin (A7030), immunoglobulin G

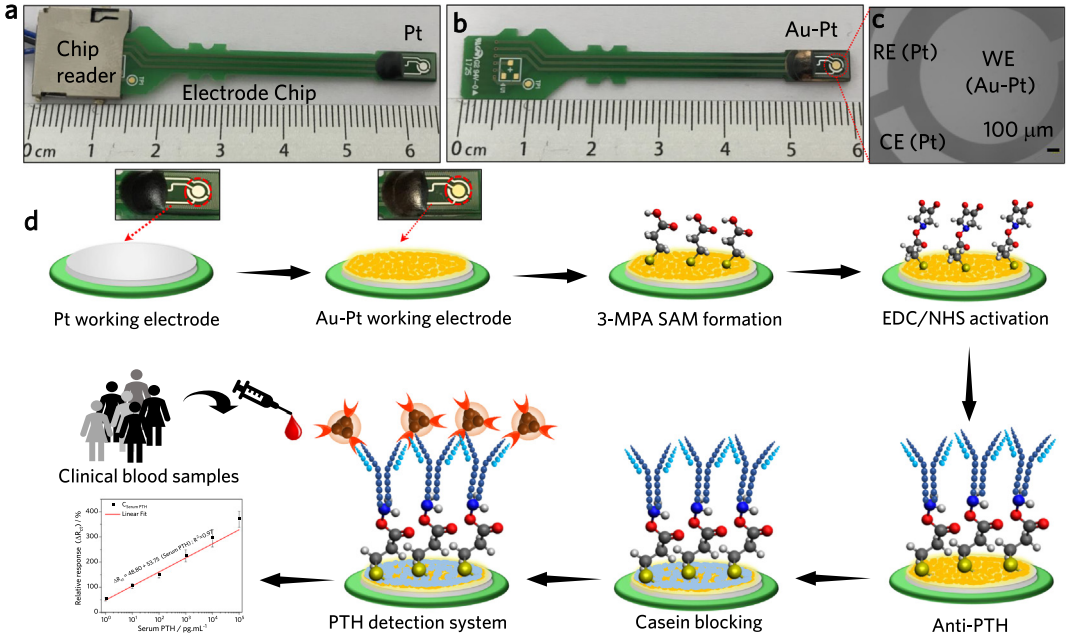

Fig. 1. (a) The digital picture shows the fabricated Pt disk electrodes coupled with the chip reader in three electrode configurations on the PCB circuit (b) shows the digital photograph of Au-Pt modified hybrid electrode. The working electrode radius was 1 mm surrounded with Pt counter and a Pt reference electrode. (c) An optical microscopic image shows the sensing area of the fabricated sensor. (d) The schematic diagram shows the binding mechanism of PTH in serum with corresponding PTH antibodies immobilized on Au-Pt electrodes towards electrochemical PTH sensor.

(≥ 95% IgG, 56,834), C-reactive protein (CRP, C1617), casein from bovine milk (C7078) and 2-(N-morpholino) ethanesulfonic acid (MES, ≥ 99%) were purchased from Sigma Aldrich. Anti-PTHLH antibody conjugated to biotin (ab82799) was purchased from Abcam. 1-Step Ultra TMB-ELISA (34028) reagents were purchased from Thermo Fisher Scientific and used without purification. 4-(2-hydroxyethyl)-1-piperazineethanesulfonic acid (HEPES) solution was purchased from Biosesang, Inc. (H2003-1). Phosphate buffered solution (PBS, 0.1 M, pH 7.4) used in this work was prepared using 0.1 M $Na_2HPO_4.12H_2O$, 0.1 M $NaH_2PO_4.2H_2O$, and 0.1 M KCl. All solutions were prepared using Milli-Q water (18 MΩ cm^{-1}). For practical PoC testing, serum samples from patients with cancer and from cancer-free individuals were assayed ($n = 20$) using the fabricated electrode sensor and compared with results from the commercial system Roche Cobas 8000 (Roche Diagnostics, Germany). All other reagents were of analytical reagent grade or the highest purity available and used without any further purification unless indicated otherwise.

2.2. Pt electrode fabrication and formation of nanostructured au

Au disk electrodes and necessary transmission lines were fabricated on printed circuit board (PCB) by standard lithography methods. Each electrode combination comprised of working, counter and reference electrode respectively and featured one customized readout circuit connection per electrode chip. The electrode fabrication included standard procedures including spin coating of photoresist, patterning, lift off, and passivation. This process resulted in a circular Pt disk electrode with a diameter of 1 mm surrounded by the counter and reference electrodes. For nanostructured Au formation on Pt disk electrodes, the Pt electrodes were initially cleaned by successive ultrasonication in isopropyl alcohol (IPA, 2 min), ethanol (EtOH, 5 min), and copious amounts of Milli-Q water. The surfaces were then dried using nitrogen. The cleaned electrodes were treated with O_2 plasma at 50 W, at 1×10^{-2} Torr for 10 s. (CUTE, Femto Science, South Korea). Before any modification of the working electrode took place, the counter and reference electrodes were covered with adhesive tape, leaving only the working electrode exposed. To avoid any formation of nanostructures on the counter (CE) and pseudo-reference electrodes (RE), passivation was necessary. Also, this method of passivation was used in later modification steps for monolayer formation and binding of antibody. The passivated electrodes were submerged in a solution containing 5 mM $HAuCl_4$ and 0.6% (v/v) NH_4OH under vigorous agitation for 2 min. After washing with deionized water, the electrodes were then immersed in 1 mM $NaBH_4$ solution (10 mL) for 5 min. Then, the electrodes were rinsed with deionized water and again transferred into a solution containing $HAuCl_4$ and NH_2OH in equimolar concentrations (1:1) of either 0.1, 1 or 10 mM for 10 min shaking and 10 min still condition to grow the Seeded nanoparticles grew into porous nanostructures. Subsequently, the electrodes were rinsed with DI water, dried in a N_2 stream and stored at room temperature until further use or modification.

2.3. Electrode characterization

Optical images of the sensing area were obtained with a CELENA S Digital Imaging System (logos biosystem, South Korea). The surface topography of the electrodeposited surfaces was examined by field emission scanning electron microscopy (FESEM) using a Carl Zeiss Sigma operated at 5 kV.

2.4. Electrode modifications

First, the Au-Pt electrodes were modified with 100 mM 3-mercaptopropionic acid in EtOH for 90 min. After washing thoroughly with ethanol and DI water, the electrodes were immersed in an aqueous solution of 25 mg.mL^{-1} EDC and 30 mg.mL^{-1} NHS in 100 mM MES buffer at pH 5.0 for 40 min after which 40 μL of 10 μg.mL^{-1} anti-parathyroid hormone antibody in 1 mM PBS, (pH 7.4) was spread onto the electrodes and left to incubate in a humid chamber for 1 h. After the anti-PTH was immobilized on Au-Pt surface via the classical EDC/NHS conjugation reaction between –COOH groups of 3-MPA and residual amino groups of antibodies, the electrodes were gently rinsed with PBS and 20 μL of casein (1 ng.mL^{-1}) were drop cast onto each electrode sensor followed by incubation at 4 °C for 1 h to avoid non-specific binding. After each step to construct the PTH detection surface, EIS and DPV measurements were conducted to monitor characteristic changes.

2.5. Electrochemical characterization

Cyclic voltammetry (CV), DPV and EIS were performed on an IVIUM CompactStat (Netherlands) at room temperature (25 °C). All experiments were carried out using a conventional three-electrode system, with modified Au-Pt as a working electrode and Pt electrodes were as counter and pseudo-reference electrodes. First, CVs were recorded in a potential window of 0.4 to −0.4 V at a scan rate of 50 mV.s^{-1} in a solution of 10 mM $[Fe(CN)_6]^{3-}/[Fe(CN)_6]^{4-}$ (1:1) and 0.1 M KCl with all the Au-Pt electrodes formed at different concentrations of $HAuCl_4$. The electrochemically active nanostructured Au surface area was determined using the Randles-Sevcik Eq. [36]. The k^0 values were estimated from the peak-to-peak separation in the voltammogram (10–250 mV.s^{-1}) using the Nicholson method [36]. DPV parameters were adjusted to a scan rate of 50 mV.s^{-1}, 10 mV pulse amplitude, 10 ms pulse width in a 0.4 to −0.2 V potential window. All potentials were referenced with a pseudo-Pt electrode fabricated on the electrode chip. EIS was measured using Au-Pt electrodes consisting of working and counter electrodes in a solution of 10 mM $[Fe(CN)_6]^{3-}/[Fe(CN)_6]^{4-}$ (1:1) and 0.1 M KCl, with an AC voltage of 10 mV, in the frequency range of 100 kHz – 0.1 Hz at each step of interface formation. The input bias potential (E_{in}) was estimated from CV analysis from 0.4 to −0.4 V for 10 cycles at a scan rate of 50 mV.s^{-1} as $E_{in} = (E_{ox} + E_{red})/2$, where E_{ox} and E_{red} are the oxidation and reduction peak potentials respectively. The electrochemical properties were obtained by fitting with a modified Randle's circuit using the commercially available software ZView® (Scribner Associates Inc., Southern Pines, NC, USA).

2.6. Electrochemical PTH detection

The anti-PTH modified Au-Pt electrodes were immersed for 30 min into both PBS and serum containing PTH at concentrations from 1 to 10^5 pg.mL^{-1}. After rinsing with PBS, EIS and DPV measurements were performed as described above. To test the specificity of the immunosensor, it was incubated with a solution of the following possible interferants: thyroid stimulating hormone (TSH), human serum albumin (HSA), triiodothyronine (T_3), C-reactive protein (CRP), and bovine serum albumin (BSA). Each protein was prepared in a concentration of 1 μg.mL^{-1} and 30 μL were used to cover electrodes for 30 min incubation. Subsequently, electrodes were rinsed with PBS, and impedance spectra were recorded. Serum samples of 20 subjects were acquired under informed consent from EONE laboratories (Incheon, South Korea), and PTH levels were evaluated by drop casting 30 μL of serum on the developed Au-Pt hybrid electrodes followed by 30 min incubation. After washing with 10 mM PBS, the obtained EIS results were analyzed and compared with the commonly used electrochemical immunoassay device Cobas 8000, (Roche Diagnostics).

Prior to commencing the study, this study protocol, amendments, and informed consent procedures were approved by the Institutional Review Board and the research ethics committees of Ewon Laboratories (IRB No. 128477–201,611-ER-010). The study was conducted in compliance with the protocol, the current revision of the Declaration of Helsinki, Good Clinical Practice, the applicable regulatory requirements,

and all the relevant guidelines of the International Conference for Harmonization. Before exposure to any study-related procedures, all patients gave their written informed consent. Patients were informed by the investigator about the aims, methods, anticipated benefits, and potential hazards of participating in the study.

2.7. PTH detection with ELISA

The ELISA test was performed similarly to a previously described protocol [37]. Briefly, each well of the microplate was coated with capture antibody (mouse monoclonal PTH antibody (10 μg. mL^{-1}) diluted in PBS buffer (0.1 M, pH 7.4) and incubated overnight at room temperature. The next day, the plate was washed three times with PBS containing 0.05% (*w*/*v*) polyoxyethylene sorbitan monolaurate (TWEEN-20) (PBST). Next, wells were blocked with100 μL of 5% (w/v) casein in 0.1 M PBS, for 60 min at room temperature, after which the plate was once again washed three times with PBST. Subsequently, the wells were filled with serially diluted PTH antigen in 10 mM PBS and incubated at 37 °C for 1 h after which followed again washing with PBST. Additionally, IgG capture antibody was diluted in 10 mM PBS and incubated in the ELISA plate as a negative control. After washing with PBST, horseradish peroxidase (1:5000 in 0.1 M PBS) was conjugated with anti-PTHLH antibody (in 100 μg. mL^{-1} BSA, 10 mM HEPES (pH 7.4), 10 mM NaCl, 0.05% (*w*/*v*) Tween-20 in 0.1 M PBS) was added and incubated at 37 °C for 30 min. After washing, the plate was incubated with TMB substrate at room temperature for 15 min, and the absorbance was measured at 650 nm using a 96-well microplate reader.

3. Results and discussion

3.1. Formations of au nanostructures on Pt disk electrode surface

The digital pictures shown in Fig. 2(a) describe the series of steps involved in the fabrication of Au on Pt disk electrodes. The working electrode (WE) remained exposed, while all other areas were covered with adhesive tape to limit the solution phase growth of Au structures precisely to the WE and avoid any formations on the counter, reference, and other areas in the vicinity. This method of Au nanostructure formation can be applied to all surfaces either conducting or insulating such as glass, PDMS, or plastic. This insulation of the WE also enables selective functionalization of the transducer surface with self-assembled monolayers (SAM) and subsequent analyte immobilization selectively on the Au-Pt surface. The surface of the bare disk electrode revealed an apparent smooth surface by SEM imaging as displayed in Fig. 2(b). Nanostructured Au films formed on the electrodes to enhance the electron transfer exchange rates compared to bare Pt disk electrodes which were expected to significantly enhance the sensitivity of the electrochemical sensor [38]. The preparation of Au nanostructures on disk electrodes via chemical route involved three steps; (*i*) seeding of Au precursors, (*ii*) reduction into Au^0 clusters and (*iii*) growth by hydroxylamine reduction of $HAuCl_4$. Seeding was accomplished by the addition of ammonium hydroxide (NH_4OH) into a solution of $HAuCl_4$ on passivated disk electrodes. Addition of NH_4OH immediately turned the solution colour into orange and caused a rapid deposition of Au^{3+} species onto the surface. These Au^{3+} precipitates were subsequently reduced into Au^0 nanoparticles by $NaBH_4$. This reduction step was necessary to allow further growth of nanostructures. Subsequently, the NH_2OH

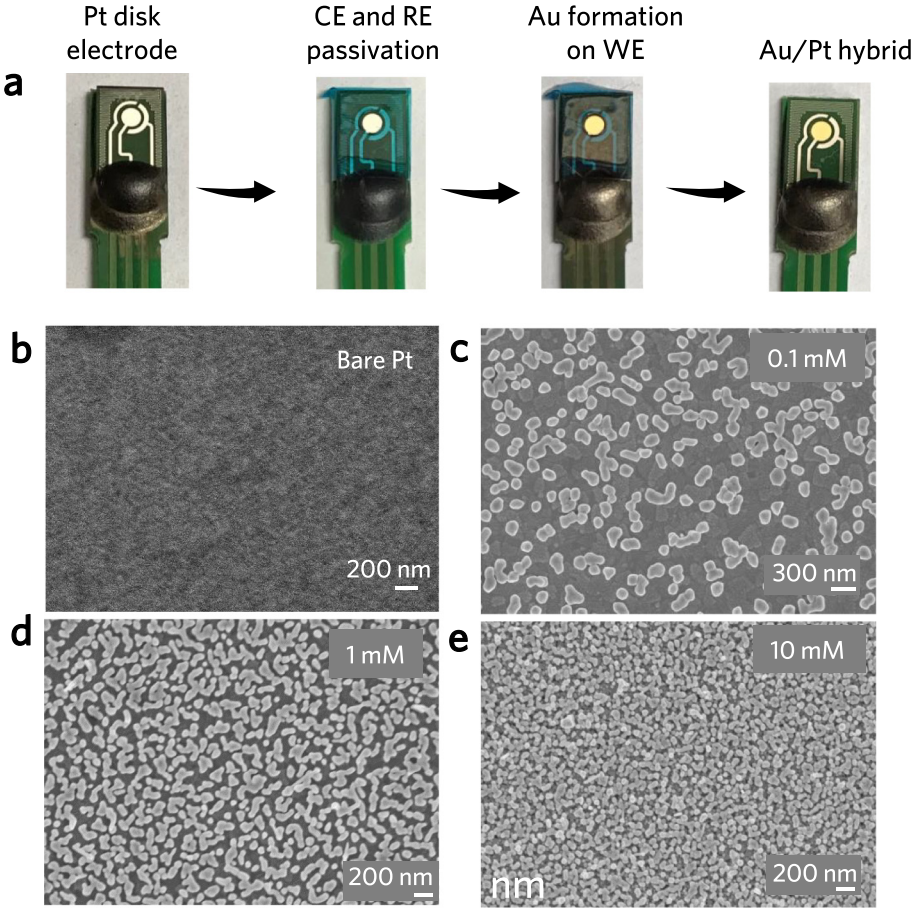

Fig. 2. (a) Digital pictures shows the bare Pt disk electrode, passivation of Pt counter and Pt reference electrodes, subsequent Au nanostructure formations, and formation of Au-Pt hybrid disk electrode. Scanning electron microscopic images of (b) bare Pt and nanostructured Au formations with different concentrations of Au with (c) 0.1 mM, (d) 1 mM, and (e) 10 mM $HAuCl_4$ with equimolar NH_2OH (1:1) respectively.

medicated growth with a conc. of 0.1 mM $HAuCl_4$ substrate resulted in a low density of Au nanostructures. Increasing the $HAuCl_4$ concentration to 1 mM and 10 mM resulted in higher coverage with porous like Au structures. These formations were confirmed by SEM analysis shown in Fig. 2(c-e).

Nyquist plots were observed recorded by EIS using the $[Fe(CN)_6]^{3-/4-}$ redox probe as described above to examine the interfacial properties of the electrode like conductivity and electrocatalytic features before and after modifications [39]. The semi-circular region at higher frequencies indicates an electron transfer limited process, and the straight line at lower frequencies is due to the limited mass transfer of $[Fe(CN)_6]^{3-/4-}$ ions. As displayed in Fig. 3(a), the bare Pt disk shows a well-defined, enlarged semi-circle with a charge transfer resistance (R_{ct}) of 8 kΩ. However, the diameter of the semi-circle in the Nyquist plot of the Au disk electrode decreases dramatically for 0.1, 1, and 10 mM Au formations resulting in lower R_{ct} of 6.3 kΩ, 1.8 kΩ, and 180 Ω respectively. The electrodes which underwent modification with 10 mM $HAuCl_4$ showed porous nanostructures and the highest conductivity among all electrodes in the present study with a nearly straight line in EIS spectra. The decrease in R_{ct} confirms that the modifications enhanced the surface area providing better conduction pathways to promote electron transfer. We further investigated the electrochemical properties of the $[Fe(CN)_6]^{3-/4-}$ redox couple at the formed Au-Pt electrodes. Fig. 3(b) compares the CVs for 10 mM $[Fe(CN)_6]^{3-/4-}$ in 0.1 M KCl solution obtained at bare Pt, and Au modified electrodes. At the bare Pt electrode, one pair of well-defined redox peaks was obtained, which was ascribed to the one-electron transfer process of $[Fe(CN)_6]^{3-/4-}$ at the electrode with anodic (I_{pa}) and cathodic peak (I_{pc}) currents of 3.87 and − 3.93 μA, respectively. Subsequently, the electrodes produced at increasing Au concentrations showed larger peak currents (I_{pa}: 4.50, 5.47, and 7.28 μA; I_{pc}: −4.51, −5.50, and − 7.56 μA respectively) than the bare Pt electrode, suggesting that deposited electrodes possessed excellent electrical conductivity. A relative response (RR%) in current enhancement (ΔI) of 88.1% in I_{pa} which was calculated as follows,

$$RR\%(\Delta I) = \frac{(I - I_0)}{I_0} \times 100 \quad (1)$$

Where ΔI is current enhancement ratio; I_0 and I are the peak current values (I_{pa} and I_{pc}) before and after modification of the electrode surface. The improvement is due to the increased surface area of the electrode in comparison to a bare Pt electrode. Also, the effect of the scan rate on all the electrodes was elucidated and presented for the bare Pt, and Au-Pt electrode as shown in Fig. 3(c-f). Both cathodic and anodic peak currents were found linearly increasing

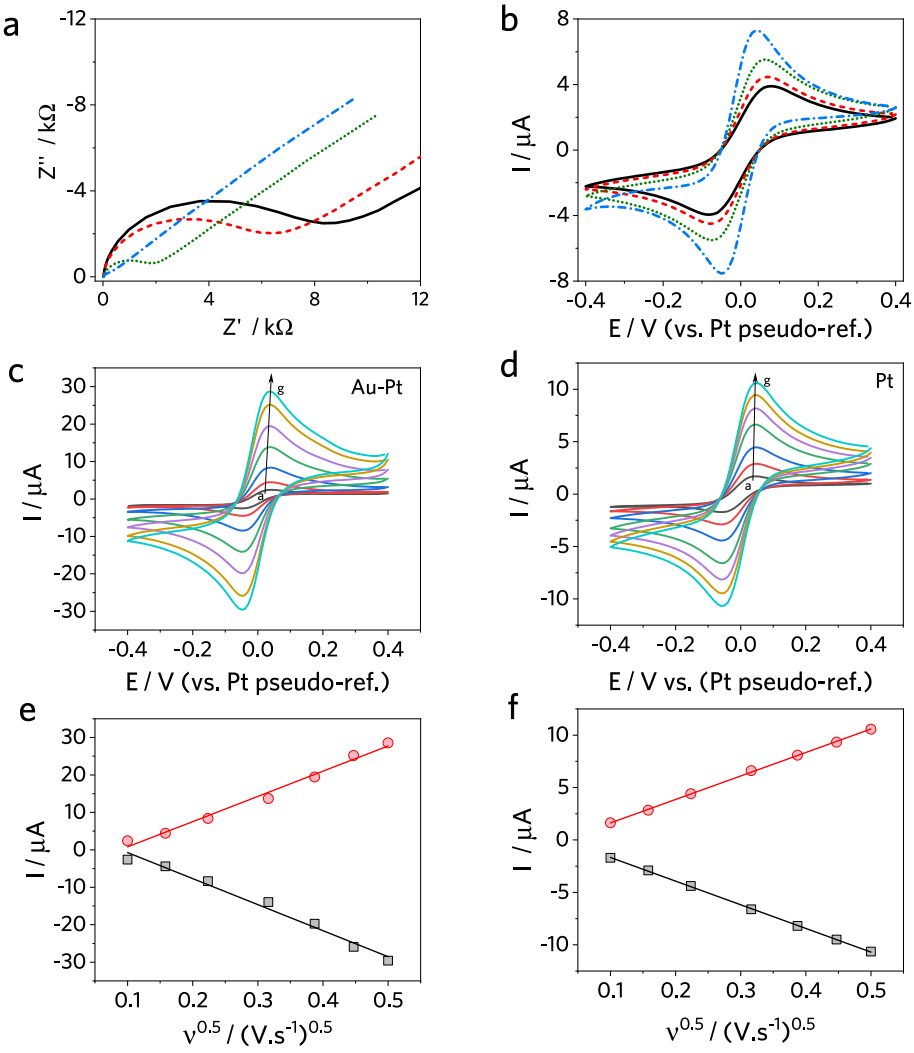

Fig. 3. (a) Electrochemical impedance spectra and (b) cyclic voltammograms of bare Pt (—) along with Au-Pt electrode formed at 0.1 (- - -), 1 (....), and 10 mM (-.-.-) $HAuCl_4$ measured in potential window of 0.4 to −0.4 V with a scan rate of 50 $mV.s^{-1}$. (c,d) cyclic voltammogram of Au-Pt and Pt electrodes in 10 mM $[Fe(CN)_6]^{3-/4-}$ at varying scan rates and inset a to g indicates the scan rates from 10, 25, 50, 100,150, 200 and 250 $mV.s^{-1}$ respectively. (e,f) Randles-Sevcik plot shows the cathodic ($I_{pc;}$ ■) and anodic ($I_{pa;}$ ●) peak currents vs. (scan rate)$^{0.5}$ of Au-Pt and Pt electrodes vs Pt pseudo-reference electrode in 10 mM $[Fe(CN)_6]^{3-/4-}$ at varying scan rates from 10 to 250 $mV.s^{-1}$.

with increasing potential scan rate and were linear with the square root of scan rate in the range from 10 to 250 mV.s^{-1}, indicating a diffusion controlled redox process of $[Fe(CN)_6]^{3-/4-}$ at the electrode. The electrochemically active Au surface area determined by the Randles-Sevcik plot was 0.157 cm^2, which is double the physical area (0.0078 cm^2) of the bare Pt electrode. This increment resulted from the formation of nanostructures on the surface. The kinetics of the reduction/oxidation of the $[Fe(CN)_6]^{3-/4-}$ redox couple quantified by the heterogeneous electron rate constant (k^0) [40] also varied on these surfaces. Bare Pt electrodes exhibited a k^0 of 1.03 cm s^{-1} which increased to 1.28, 1.45, and 1.80 cm s^{-1} for electrodes modified with 0.1, 1 and 10 mM $HAuCl_4$ respectively. This indicates that nanostructured Au electrodes possessed faster, reversible kinetics due to faster self-exchange rates among all and it is in good agreement with the reported literature for Pt [41] and Au and Pt-Au [42] electrodes.

3.2. Simulations for electric filed distributions on Pt and Au-Pt hybrid electrodes

Electric field distributions on both clean Pt and nanostructured Au-Pt electrodes were simulated with the software COMSOL Multiphysics [43] and are shown in Fig. 4. To simulate the electric field distribution on the proposed electrode, a two-electrode model was considered which consisted of Au (σ: 4.1 × 10^7 S/m; ε_r:0.8), Pt (σ: 9.43 × 10^6 S/m; ε_r:0.73) working and counter electrodes having dimensions of ~5 μm with a thickness of 200 nm separated by a 5 μm insulation layer (polydimethylsiloxane; σ: 10^{-11} S/m; ε_r: 2.75) of same thickness and 1× PBS buffer at 20 °C (σ: 1 S/m; ε_r: 80) as an electrolyte. A stationary electric field potential of 10 mV was applied between working and counter electrodes and 1× PBS was used as a reference electrolyte. The bare Pt electrode (Fig. 4a), showed the electric field strength concentrated at the edge of the electrode indicating that the highest measurement sensitivity was limited to the side/edges of the electrode while lower sensitivity would be present at the centre of the electrode. Under the same conditions, Au-Pt electrodes additionally exhibited a strong electric field at the scattered nanostructures as well as on the electrode edge (Fig. 4b). Therefore, the formation of nanostructures increased the electric field intensity which in turn improved the overall sensitivity of the electrochemical sensor.

3.3. Electrochemical characterization of PTH sensor

EIS [44] and DPV measurements were performed to understand the electrode-electrolyte interface characteristics and to explore the surface modification properties during various steps of the impedance sensor fabrication as displayed in Fig. 4(c,d). Changes in impedance magnitude (|Z|) was observed upon modification with linkers, antibody and PTH protein markers (Fig. 4c). The nanostructured Au electrode (10 mM $HAuCl_4$) showed the lowest value of |Z|, due to the large surface area of the electrode. A huge increase in |Z| resulted from activation with 3-MPA linker which formed a uniform self-assembled monolayer on the electrode. The alkanethiol layers constrained the electron transfer due to effective repulsion of the anionic redox indicator, $[Fe(CN)_6]^{3-/4-}$ by the negatively charged carboxylate groups. The surface coverage (Θ) [45] was estimated to be 91% from the changes in charge transfer resistance (R_{ct}), using the equation $\Theta = 1 - R_{ct}/R'_{ct}$, where R_{ct} and R'_{ct} indicate the charge transfer resistance before and after SAM formation. The subsequent activation step with EDC-NHS resulted in the formation of neutral NH_2 bonds with –COOH which allowed easier penetration of $[Fe(CN)_6]^{3-/4-}$ ions towards the electrode surfaces yielding again a lower |Z| compared to the previous step. The immobilization of anti-PTH antibodies on the EDC-NHS activated surface lead to an increase of |Z| because antibodies hinder the movement of $[Fe(CN)_6]^{3-/4-}$ ions towards the electrode. Finally, the casein blocking step and subsequent PTH interactions further resulted in enhanced |Z| in the low-frequency region of the bode plots because of the formation of the antibody-PTH complex. The complex acts as an inert blocking layer against $[Fe(CN)_6]^{3-/4-}$ ions. DPV measurements, performed in parallel to EIS recordings observed for the whole modification process, showed the current variations with each modification step and agreed with EIS results as shown in Fig. 4(d). These results confirm the formation of a perfect receptive transducer interface for effective determination of PTH in serum.

3.4. Analytical performance of the immunosensor and the electrochemical detection of PTH

Under optimized experimental conditions, the analytical performance of the receptive interfaces was tested by EIS and DPV measurements with standard solutions of PTH in PBS and serum with concentrations ranging from 1 to 10^5 pg.mL^{-1} as shown in Fig. 5. The charge transfer resistance (R_{ct}) signal increased while current (i) decreased with increasing PTH concentrations. Both observed effects are

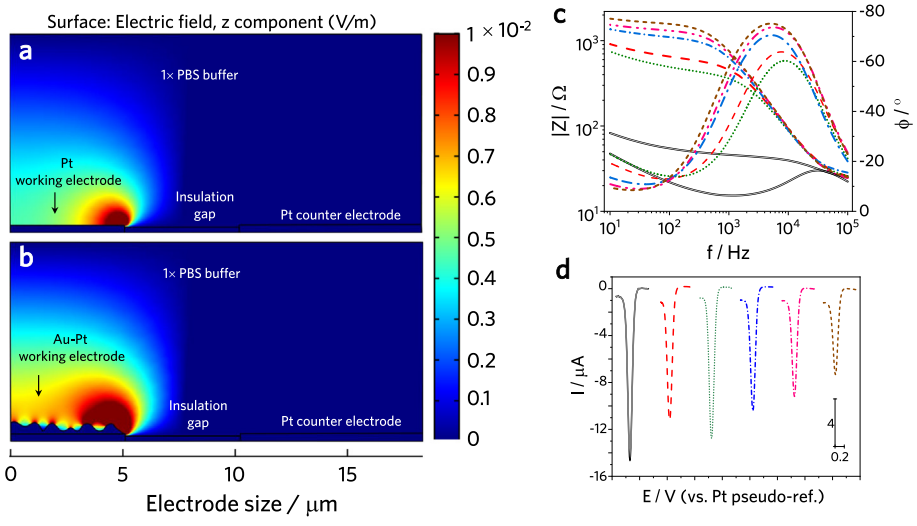

Fig. 4. Simulated electric field distributions on (a) bare Pt disk electrode and (b) Au-Pt hybrid electrodes, cross-sectional view of the electrodes was considered for simulation having working electrode length (5 μm), counter electrode (7.5 μm) with an insulation gap (5 μm) under the application of stationary electric field of 10 mV. (c) Bode plots (|Z|, ϕ vs. f) and (d) differential pulse voltammetry responses observed in 10 mM $[Fe(CN)_6]^{3-/4-}$ in 0.1 M KCl for bare Au-Pt (==) and after SAM formation of 3-MPA (— —, 100 mM), EDC-NHS (...., 130 mM–260 mM), ab-PTH (—.-, 1 μg.mL^{-1}) and Casein (—..-, 5 ng.mL^{-1}) on the Au-Pt hybrid electrodes for PTH (- - -, 10 pg.mL^{-1}) binding confirmation.

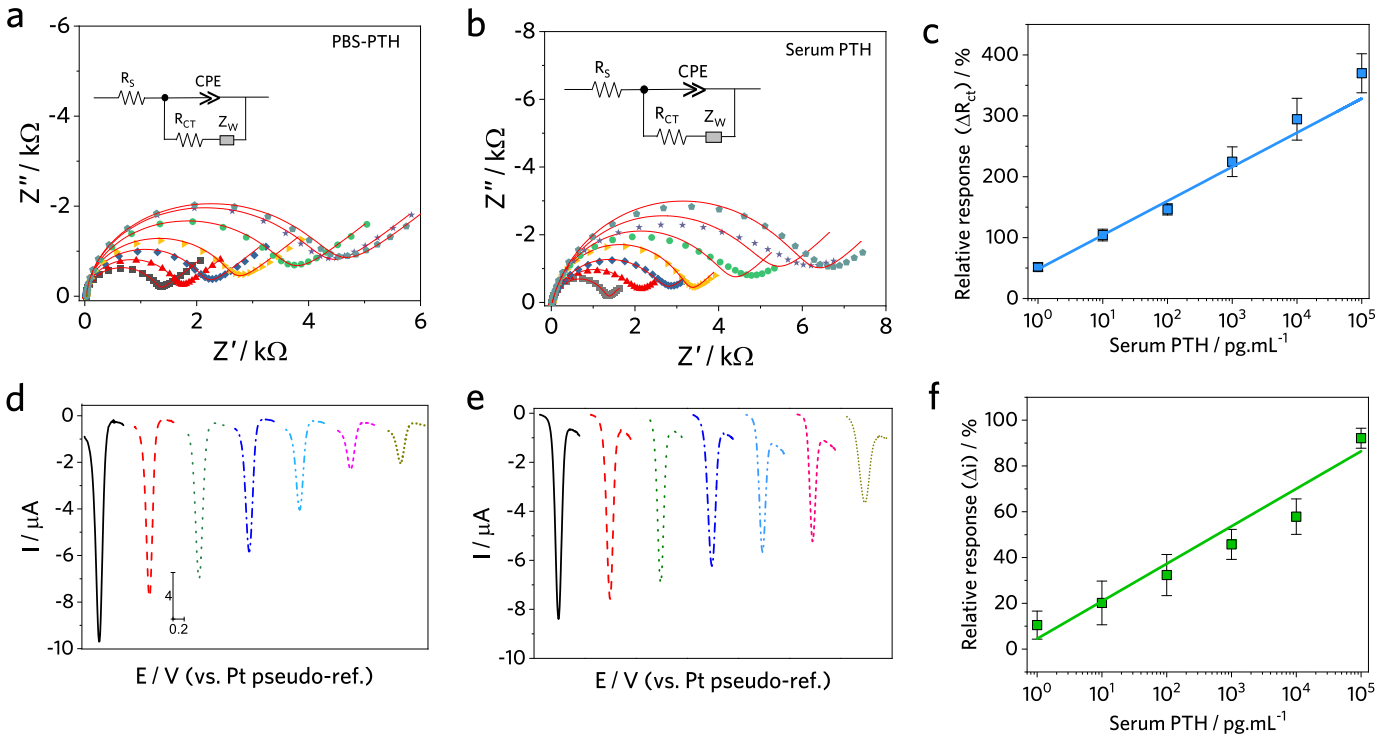

Fig. 5. Nyquist plots (Z′ vs. Z′′) obtained for different concentration of (a) PTH in PBS ($C_{PBS\text{-}PTH}$) and (b) PTH in human serum ($C_{Serum\ PTH}$) for blank (■), 1(▲), 10(♦), 100(►), 1000(●), 10,000(★), 100,000 (⬟) pg. mL^{-1} with solid lines indicate the fitting with equivalent circuit respectively. Data were expressed as the mean of four replicated measurements and fitted with Randle's circuit model as illustrated in the *inset* in (a,b). DPV responses observed for (d) PTH detection in PBS ($C_{PBS\text{-}PTH}$) and (e) PTH in human serum ($C_{Serum\ PTH}$) samples within the potential window of −0.3 to 0.4 V for blank (—), 1 (— —), 10 (…), 100 (—.-), 1000 (—..-), 10,000 (— — -), 100,000 (….) pg.mL^{-1} concentrations PTH. Calibration curves for both methods indicating relative response (RR%) w.r.t to PTH concentrations shown in (c) RR% (ΔR_{ct}) vs. $C_{PTH\text{-}serum}$ with a calibration curve $\Delta R_{ct} = 48.80 + 53.75$ (serum PTH); $R^2 = 0.97$, and (f) RR% (Δi) vs. $C_{PTH\text{-}serum}$ with a calibration curve $\Delta i = 4.51 + 16.38$ (serum PTH); $R^2 = 0.973$ respectively. Data points (■) are represented as mean ± S.D. of four replicated measurements fitted with a linear regression line (—).

directly connected to a decrease in the number of binding sites on the receptive molecular layer which is due to an increase in steric blockage of the surface caused by PTH binding, overall resulting in suppression of electron transfer (Fig. 5(a,b,d,e)). The extracted values from the impedance fitting in Fig. 5(a,b) are shown in Tables 1 and 2. The relative response (RR%) was used as measurand for the detection and the quantification of antigen-antibody reactions in both EIS and DPV assays:

$$RR\% = \frac{(R_{antigen} - R_{blank})}{R_{blank}} \times 100 \quad (2)$$

Here, R_{blank} is the response (R_{ct} or i) of the electrode with immobilized antibodies without PTH bound, while $R_{antigen}$ is the response (R_{ct} or i) value after incubation with solutions of different PTH concentrations. A calibration curve was constructed using the relationship between the RR% and the logarithmic concentration of PTH over the full range. The RR% response was evaluated with both analytical methods, and a linear range of 1–10,000 pg.mL^{-1} was obtained with logarithmic PTH concentrations in serum. A good linear relationship was obtained between RR% with logarithmic concentrations of PTH in serum as shown in Fig. 5c. The regression equation is RR% (ΔR_{ct}) = 53.75 ×log[PTH] (pg.mL^{-1}) + 48.8 and the correlation coefficient r = 0.983 with a detection limit of (LOD) 0.36 pg.mL^{-1} based on $3 \times \sigma/S$, where σ is the standard deviation from the blank samples and S is the slope of the curve [46]. Similarly, as expected, the DPV peak current decreases with an increase in the concentration of PTH. A good linear relationship was obtained between RR% (Δi) and the logarithm of PTH concentrations in serum in the range from 1 to 10,000 pg.mL^{-1}. The regression equation is RR%(Δi) = 16.38 × log [$C_{Serum\ PTH}$] (pg. mL^{-1}) + 4.51 and r = 0.978 (Fig. 5f). The limit of detection (LOD) was found to be 0.59 pg.mL^{-1} which is well below the normal range (10–69 pg. mL^{-1}) of PTH in the human body [47]. Further, the analytical performance of the developed sensor was compared with previous reports on PTH detection from the literature and is shown in Table 4. The sensitivity in PTH detection by EIS and DPV measurements were evaluated to be 0.163% and 0.17% per decade respectively. Furthermore, the accuracy

Table 1
Extrapolated values of the equivalent circuit elements obtained by fitting the experimental results of various concentrations of PTH antigen in PBS from the Nyquist plots as shown in Fig. 5a.

PTH (pg.mL^{-1})	R_s (Ω)	CPE		R_{ct} (Ω)
		T (×10^{-7} Ω^{-1}. s^P)	P	
Blank	22.1 ± 0.1	2.1 ± 0.5	0.98 ± 0.002	1349 ± 5.9
1	23.0 ± 0.1	2.0 ± 0.6	0.98 ± 0.002	1703 ± 9.7
10	24.1 ± 0.1	2.2 ± 0.6	0.97 ± 0.002	2263 ± 12.5
100	26.8 ± 0.1	2.4 ± 0.6	0.96 ± 0.002	2762 ± 16.7
10,000	29.3 ± 0.2	2.5 ± 0.6	0.96 ± 0.002	3761 ± 23.5
100,000	31.3 ± 0.2	2.5 ± 0.6	0.96 ± 0.002	4432 ± 29.7
1,000,000	32.1 ± 0.2	2.5 ± 0.7	0.96 ± 0.002	4660 ± 32.9

Table 2
Extrapolated values of the equivalent circuit elements obtained by fitting the experimental results of various concentrations of PTH antigen in Human Serum from the Nyquist plots as shown in Fig. 5b.

PTH (pg.mL^{-1})	R_s (Ω)	CPE		R_{ct} (Ω)
		T (×10^{-7} Ω^{-1}. s^P)	P	
Blank	35.3 ± 0.8	3.3 ± 0.2	0.89 ± 0.007	1365 ± 6.9
1	45.0 ± 1.1	4.2 ± 0.3	0.83 ± 0.007	2169 ± 10.7
10	46.6 ± 1.2	4.8 ± 0.3	0.82 ± 0.006	2791 ± 13.1
100	47.0 ± 1.0	5.2 ± 0.7	0.89 ± 0.005	3369 ± 12.7
10,000	49.2 ± 0.9	5.5 ± 0.1	0.84 ± 0.005	4344 ± 16.1
100,000	54.6 ± 1.4	5.5 ± 0.1	0.84 ± 0.006	5393 ± 29.4
1,000,000	56.1 ± 1.5	5.6 ± 0.1	0.84 ± 0.005	6380 ± 27.9

Table 3
Comparison of the PTH biomarker sensing efficiency in PBS (pH. 7.0) and serum samples.

	EIS		DPV	
	PBS	Serum	PBS	Serum
Linear range (pg.mL^{-1})	1–10,000	1–10,000	1–10,000	1–10,000
LOD (pg.mL^{-1})	0.15	0.36	0.23	0.59
R^2	0.985	0.978	0.980	0.976
RSD (%)	3 ± 2	8 ± 4	4 ± 2	7 ± 3
Sensitivity (% decade^{-1})	0.522	0.163	0.26	0.17
K_a (pg.mL^{-1})	0.46	0.62	0.43	0.8
K_d (pg.mL^{-1})	2.2	1.7	2.4	1.3
Intra-day (%)	3.2	3.8	4.6	5.4
Inter-day (%)	5.7	6.5	5.9	7.5

of the PTH sensors was evaluated by conducting experiments by both EIS and DPV methods on three different nanostructured SD card electrodes, each of them measured twice to acquire a relative standard deviation (RSD) for each PTH measurement performed. The binding affinity constant (K_a) was calculated using the Langmuir isotherm approach, where the model assumes equal binding energy for all binding sites [48]. Briefly, in the proposed experiments, the change in R_{ct} can be related to the binding energy of PTH with anti-PTH given by the Eq. (3),

$$\theta = 1 - \frac{R_{ct}(C_0)}{R_{ct}(C_i)} \tag{3}$$

where θ is the occupied binding sites, $R_{ct}(C_0)$and $R_{ct}(C_i)$ are charge transfer resistance at PTH concentrations of zero and above-zero respectively.

θ can then be related to the association constant as.

$$\theta = 1 - \frac{K_a C}{1 + K_a C} \tag{4}$$

where K_a is the association constant and C is the concentration of the solution. Eq. (4) can be rearranged to

$$K_a C = \frac{\theta}{1-\theta} \tag{5}$$

Thus from (4) and (5)

$$K_a C = \frac{R_{ct}(C_i) - R_{ct}(C_0)}{R_{ct}(C_0)} = \frac{\Delta R_{ct}}{R_{ct}(C_0)} \tag{6}$$

Using Eq. (6), a curve was plotted between $\frac{\Delta R_{ct}}{R_{ct}(C_0)}$ and the concentration of PTH, which reveals that $\frac{\Delta R_{ct}}{R_{ct}(C_0)}$ varies linearly with the concentration and a linear equation $\frac{\Delta R_{ct}}{R_{ct}(C_0)} = 0.37 + 0.62\ \log C_{Serum\ PTH}\ (pg.mL^{-1})$ was obtained with a correlation coefficient of 0.98. Similarly, for DPV analysis, a linear equation $\frac{\Delta I}{I_0} = 0.9 + 0.8\ \log C_{Serum\ PTH}\ (pg.mL^{-1})$ was obtained with a correlation coefficient of 0.97. From this, K_a was estimated as the slope of the regression equation as 0.62 and 0.8 pg.mL^{-1} for both EIS and DPV measurements. Similarly, the dissociation constant (K_d) was evaluated from the plot of different concentration of PTH in both PBS and serum (C_{PTH}) versus C_{PTH} / ΔR_{ct} (ΔI) [49]. Subsequently, K_d could be obtained by dividing the *y*-intercept by the slope of the linear regression curve. The analytical parameters of both EIS and DPV measurements for PTH in PBS and serum are summarized in Table 3, and both possessed similar performance towards the PTH detection in serum samples.

3.5. Selectivity, reproducibility, reliability, and validation of the accuracy of the immunosensor

The specificity of the proposed immunosensor was investigated by performing negative control experiments where the receptive interfaces were incubated with non-specific proteins TSH, albumin, T_3, CRP and IgG as interfering biomarkers ($n = 5$) along with PTH in PBS and serum samples all at the high concentration of 1 μg.mL^{-1}. As shown in Fig. 6a, the relative response (RR%) for R_{ct} against the non-specific proteins were much lower than those for PTH in PBS and serum indicating that the immunosensor exhibited high selectivity for PTH. Further, ELISA experiments were performed with PTH antigen and two antibodies and compared with the EIS method to determine the sensitivity of the assay (Fig. 6b). The absorbance observed from different concentrations of PTH increased and fitted with a linear regression line, A = 0.008 ×log [$C_{Serum\ PTH}$] (pg.mL^{-1}) + 0.05, with $R^2 = 0.975$. Both methods showed good sensitivity for PTH detection in the range 10^0–10^5 pg.mL^{-1} with EIS showing better linearity than ELISA which is an added advantage for PoC applications.

Furthermore, to achieve high reproducibility from the developed nanostructure-based electrode sensors and to avoid any inter and intraassay variations during PTH detection, electrodes with the same R_{ct} were chosen and utilized for further experiments. The stability of the immunosensors after storage at 4 °C in 10 mM PBS, pH 7.4, was tested by observing the changes in the impedance magnitude. The constructed immunosensors still kept 83.6% of their initial response for 1000 pg.mL^{-1} after storage at 4 °C for 10 days which indicated satisfactory stability.

The change in charge transfer resistance (ΔR_{ct}) was used as an analytical parameter for the detection of PTH in patient serum and was compared to results obtained with the Roche Cobas system. Differences in PTH levels between cancer patients and cancer-free patients were observed where cancer patients possessed higher amounts of PTH up to 254 pg.mL^{-1} compared to healthy individuals (63.9 pg.mL^{-1}).

Table 4
Analytical characteristics of different PTH immunosensors as reported in the literature.

Transducer matrix	Method	Sample	Linear range (pg.mL^{-1})	LOD (pg.mL^{-1})	Reference
PAMAM[a] dendrimers	EIS	Artificial serum	0.01–0.06	0.00143	[50]
Au electrode	EIS, CV[d]	Artificial serum	0.1–0.6	0.0001	[51]
Au electrode	EIS	Artificial serum	10–50	7.65	[52]
MoS_2-Graphene/Au electrode	CV	Serum	1–50	–	[53]
Membrane based assay	DPV	Serum	5–5000	1	[54]
AuNPs	LFIA[e]	Serum	–	6.60	[55]
Magnetic particles	ELISA	Serum	–	94.3	[56]
Au IDE[b]/FET[c]	Electrical	Fetal bovine serum	–	0.45	[57]
Au nanostructured electrode	EIS, DPV	Serum	10–10,000	0.36	Present work

[a] PAMAM: Poly(amidoamine).
[b] IDE: Interdigitated electrode.
[c] FET: Field effect transistor.
[d] CV: Cyclic voltammetry.
[e] LFIA: Lateral flow immunoassay.

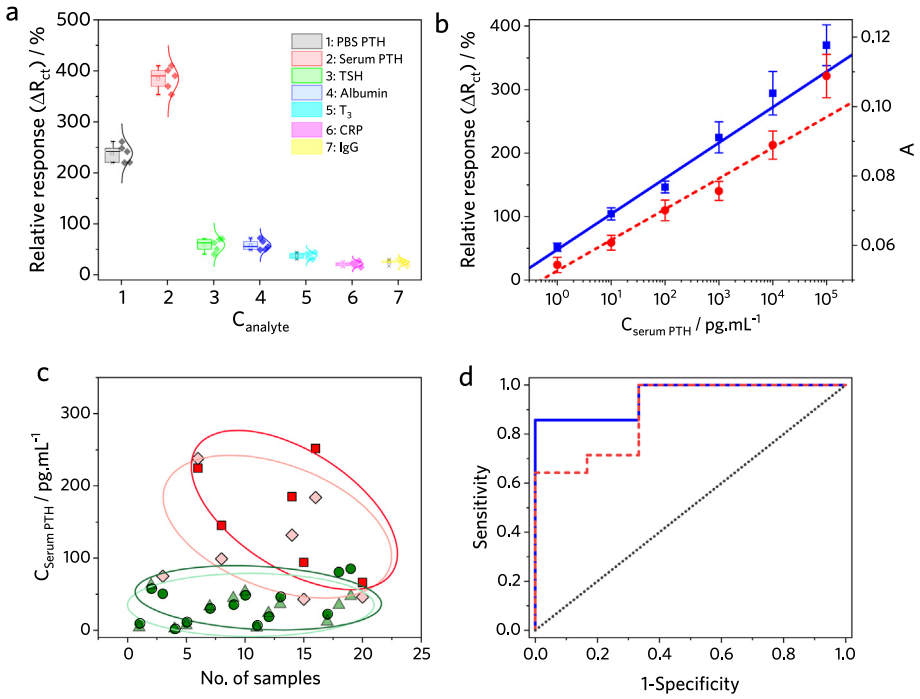

Fig. 6. (a) Relative response % (ΔR_{ct}) observed for different analytes (PBS-PTH, serum PTH, TSH, Albumin, T_3, CRP and IgG) all at same concentration level (1 μg.mL^{-1}) with the developed immunosensor; (b) Comparison of the relative response % (ΔR_{ct}) of the immunosensor with absorbance observed from ELISA for different concentrations of serum PTH (1 to 10^5 pg.mL^{-1}). Data points (■, ○) are fitted with a linear regression line (—, ...) for both EIS and ELISA methods with a regression curve $\Delta R_{ct} = 48.80 + 53.75$ ($C_{Serum\ PTH}$); $R = 0.983$ and $A = 0.05 + 0.008$ ($C_{Serum\ PTH}$); $R = 0.975$, respectively. (c) Comparison of the proposed sensor with commercially available equipment (Roche Cobas 8000 system) for accurate quantification of serum PTH with EIS (●: healthy, ■: disease) and Roche Cobas (▲: healthy, ♦: disease) based electrochemiluminescence methods, respectively; (d) Receiver operating characteristic (ROC) curves for EIS and Roche Cobas methods with AUC of 0.95 for EIS (—) and 0.89 for Roche Cobas (.....) respectively.

Both assays detected similar levels of PTH and test hypothesis (null and alternative) at 0.05 level when the variance is assumed = and ≠ in both tests, indicating no significant difference between the two methods (Fig. 6c). The immunosensor detected few PTH samples as high that were estimated a low by the Roche Cobas. Thus, these results confirm the accuracy of the developed immunosensor using Au-Pt hybrid electrode sensor. Data were also analyzed using a receiver operating characteristic (ROC) plot to predict diagnostic accuracy. Here, sensitivity (true positive response) is plotted against 1-specificity (false positive response) for different cutoff points (Fig. 6d). It is familiar that, a ROC curve that passes through the upper left corner provides 100% sensitivity, and 100% selectivity and the area under the ROC curve (AUC, which indicates the degree/measure of separability) quantifies the overall ability of the test to discriminate between normal and cancer samples. For clinical sample ($n = 20$) analysis, the ROC plot has an AUC value of 0.95 for EIS and 0.89 for the Roche Cobas system respectively. Further, the test results gave 83.33% clinical sensitivity and 92.85% clinical specificity using the combined EIS and Roche assay. The data indicate that more clinical samples need to be analyzed for further confirmation of the test results at a high potential for the proposed EIS method for early-stage POC testings.

4. Conclusions

In conclusion, we have demonstrated the excellent capabilities of nanostructured electrodes as highly sensitive electrochemical transducers for the detection of PTH in complex bioanalytical sensing environments. The present method offers a combination of scalable and straightforward electrode fabrication with an efficient approach for surface functionalization with anti-PTH using 3-MPA. The Au-Pt nanostructures provided abundant binding opportunities for conjugation of biorecognition elements. As a result, the constructed immunosensor exhibited a large working range of 1 pg.mL^{-1}-10 ng.mL^{-1}, and high stability with a LOD of 0.36 pg.mL^{-1} and 0.59 pg.mL^{-1} in EIS and DPV measurements respectively. The developed immunosensor was used with blood serum samples, and the results were comparable with the Roche Cobas system, and ELISA methods, implying its enormous potential for future diagnosis for biological samples in PoC applications. Further, any biorecognition element can easily be immobilized on nanostructured Au electrodes for quantitative and highly sensitive measurements in serum samples. Thus, we believe that the developed Au-Pt based hybrid chips have the potential to be directly implemented in PoC applications for the detection of protein biomarkers towards a clinical diagnostic system.

Acknowledgements

This research was supported by BioNano Health-Guard Research Center funded by the Ministry of Science and ICT (MSIT) of Korea as a Global Frontier Project (Grant number H-GUARD_2018M3A6B2057261) and by the Ministry of Trade, Industry, and Economy (Grant no. P0005440).

References

[1] W.H. He, M.L. You, W.T. Wan, F. Xu, F. Li, A. Li, Point-of-care periodontitis testing: biomarkers, current technologies, and perspectives, Trends Biotechnol. 36 (2018) 1127–1144.
[2] T.R. Kozel, A.R. Burnham-Marusich, Point-of-care testing for infectious diseases: past, present, and future, J. Clin. Microbiol. 55 (2017) 2313–2320.
[3] S. Nayak, N.R. Blumenfeld, T. Laksanasopin, S.K. Sia, Point-of-care diagnostics: recent developments in a connected age, Anal. Chem. 89 (2017) 102–123.
[4] Z.D. Li, F. Li, Y. Xing, Z. Liu, M.L. You, Y.C. Li, T. Wen, Z.G. Qu, X.L. Li, F. Xu, Pen-on-paper strategy for point-of-care testing: rapid prototyping of fully written microfluidic biosensor, Biosens. Bioelectron. 98 (2017) 478–485.
[5] J.R. Choi, J. Hu, R.H. Tang, Y. Gong, S.S. Feng, H. Ren, T. Wen, X.J. Li, W.A.W. Abas, B. Pingguan-Murphy, F. Xu, An integrated paper-based sample-to-answer biosensor for nucleic acid testing at the point of care, Lab Chip 16 (2016) 611–621.
[6] E.T.S.G. da Silva, D.E.P. Souto, J.T.C. Barragan, J.D. Giarola, A.C.M. de Moraes, L.T. Kubota, Electrochemical biosensors in point-of-care devices: recent advances and future trends, Chemelectrochem 4 (2017) 778–794.

[7] B. Bottazzi, L. Fornasari, A. Frangolho, S. Giudicatti, A. Mantovani, F. Marabelli, G. Marchesini, P. Pellacani, R. Therisod, A. Valsesia, Multiplexed label-free optical biosensor for medical diagnostics, J. Biomed. Opt. 19 (2014).
[8] A.K. Yagati, S.G. Chavan, C. Baek, M.H. Lee, J. Min, Label-free impedance sensing of Aflatoxin B(1) with Polyaniline Nanofibers/au nanoparticle electrode Array, Sensors (Basel) 18 (2018).
[9] C.M. Cheng, A.W. Martinez, J.L. Gong, C.R. Mace, S.T. Phillips, E. Carrilho, K.A. Mirica, G.M. Whitesides, Paper-based ELISA, Angew Chem. Int. Edit 49 (2010) 4771–4774.
[10] T. Zhang, D.G. Watson, L.J. Wang, M. Abbas, L. Murdoch, L. Bashford, I. Ahmad, N.Y. Lam, A.C.F. Ng, H.Y. Leung, Application of holistic liquid chromatography-high resolution mass spectrometry based urinary metabolomics for prostate Cancer detection and biomarker discovery, PLoS One 8 (2013).
[11] E. Zeidan, S.Q. Li, Z.G. Zhou, J. Miller, M.G. Sandros, Single-multiplex detection of organ injury biomarkers using SPRi based Nano-Immunosensor, Sci. Rep. UK 6 (2016).
[12] J.L. Lucas, E.A. Tacheny, A. Ferris, M. Galusha, A.K. Srivastava, A. Ganguly, P.M. Williams, M.C. Sachs, M. Thurin, J.V. Tricoli, W. Ricker, J.C. Gildersleeve, Development and validation of a Luminex assay for detection of a predictive biomarker for PROSTVAC-VF therapy, PLoS One 12 (2017).
[13] A.W.S. Fung, M.J. Knauer, I.M. Blasutig, D.A. Colantonio, V. Kulasingam, Evaluation of electrochemiluminescence immunoassays for immunosuppressive drugs on the Roche cobas e411 analyzer, F1000Res 6 (2017) 1832.
[14] M.A. Dineva, L. Mahilum-Tapay, H. Lee, Sample preparation: a challenge in the development of point-of-care nucleic acidbased assays for resource-limited settings, Analyst 132 (2007) 1193–1199.
[15] D.W. Kimmel, G. LeBlanc, M.E. Meschievitz, D.E. Cliffel, Electrochemical sensors and biosensors, Anal. Chem. 84 (2012) 685–707.
[16] X. Ren, J.R. Yan, D. Wu, Q. Wei, Y.K. Wan, Nanobody-based Apolipoprotein E Immunosensor for point-of-care testing, ACS Sensors 2 (2017) 1267–1271.
[17] X. Ren, P. Lu, R. Feng, T. Zhang, Y. Zhang, D. Wu, Q. Wei, An ITO-based point-of-care colorimetric immunosensor for ochratoxin a detection, Talanta 188 (2018) 593–599.
[18] A.K. Yagati, M.H. Lee, J. Min, Electrochemical immunosensor for highly sensitive and quantitative detection of tumor necrosis factor-alpha in human serum, Bioelectrochemistry 122 (2018) 93–102.
[19] R.J. Forster, Microelectrodes - new dimensions in electrochemistry, Chem. Soc. Rev. 23 (1994) 289–297.
[20] A.K. Yagati, I. Park, S. Cho, J. Min, Impedimetric horseradish peroxidase sensor based on Polyaniline-Nanofiber-modified microdisk electrode arrays, Sci. Adv. Mater. 9 (2017) 1595–1602.
[21] G. Rajeev, B.P. Simon, L.F. Marsal, N.H. Voelcker, Advances in Nanoporous anodic alumina-based biosensors to detect biomarkers of clinical significance: a review, Adv. Healthc. Mater. 7 (2018).
[22] J. Patel, L. Radhakrishnan, B. Zhao, B. Uppalapati, R.C. Daniels, K.R. Ward, M.M. Collinson, Electrochemical properties of nanostructured porous gold electrodes in biofouling solutions, Anal. Chem. 85 (2013) 11610–11618.
[23] C.A.R. Chapman, H. Chen, M. Stamou, J. Biener, M.M. Biener, P.J. Lein, E. Seker, Nanoporous gold as a neural Interface coating: effects of topography, surface chemistry, and feature size, ACS Appl. Mater. Inter. 7 (2015) 7093–7100.
[24] K.C. Hu, D.X. Lan, X.M. Li, S.S. Zhang, Electrochemical DNA biosensor based on Nanoporous gold electrode and multifunctional encoded DNA-au bio Bar codes, Anal. Chem. 80 (2008) 9124–9130.
[25] Z. Matharu, P. Daggumati, L. Wang, T.S. Dorofeeva, Z.D. Li, E. Seker, Nanoporous-gold-based electrode morphology libraries for investigating structure-property relationships in nucleic acid based electrochemical biosensors, ACS Appl. Mater. Inter. 9 (2017) 12959–12966.
[26] P. Daggumati, Z. Matharu, E. Seker, Effect of Nanoporous gold thin film morphology on electrochemical DNA sensing, Anal. Chem. 87 (2015) 8149–8156.
[27] L. Yang, Y.Y. Li, Y. Zhang, D.W. Fan, X.H. Pang, Q. Wei, B. Du, 3D nanostructured palladium-functionalized Graphene-aerogel-supported Fe3O4 for enhanced Ru (bpy)(3)(2+)-based Electrochemiluminescent Immunosensing of prostate specific antigen, ACS Appl. Mater. Inter. 9 (2017) 35260–35267.
[28] L. Yang, W.J. Zhu, X. Ren, M.S. Khan, Y. Zhang, B. Du, Q. Wei, Macroporous graphene capped Fe3O4 for amplified electrochemiluminescence immunosensing of carcinoembryonic antigen detection based on CeO2@TiO2, Biosens. Bioelectron. 91 (2017) 842–848.
[29] L. Shi, X.J. Rong, Y. Wang, S.M. Ding, W.Y. Tang, High-performance and versatile electrochemical aptasensor based on self-supported nanoporous gold microelectrode and enzyme-induced signal amplification, Biosens. Bioelectron. 102 (2018) 41–48.
[30] S. Ranjbar, S. Shahrokhian, F. Nurmohammadi, Nanoporous gold as a suitable substrate for preparation of a new sensitive electrochemical aptasensor for detection of Salmonella typhimurium, Sensor Actuat B-Chem 255 (2018) 1536–1544.
[31] X. Ren, H.M. Ma, T. Zhang, Y. Zhang, T. Yan, B. Du, Q. Wei, Sulfur-doped Graphene-based immunological biosensing platform for multianalysis of Cancer biomarkers, ACS Appl. Mater. Inter. 9 (2017) 37637–37644.
[32] X. Ren, T. Zhang, D. Wu, T. Yan, X.H. Pang, B. Du, W.R. Lou, Q. Wei, Increased electrocatalyzed performance through high content potassium doped graphene matrix and aptamer tri infinite amplification labels strategy: highly sensitive for matrix metalloproteinases-2 detection, Biosens. Bioelectron. 94 (2017) 694–700.
[33] A.K. Yagati, J.C. Pyun, J. Min, S. Cho, Label-free and direct detection of C-reactive protein using reduced graphene oxide-nanoparticle hybrid impedimetric sensor, Bioelectrochemistry 107 (2016) 37–44.
[34] A.K. Yagati, Y. Choi, J. Park, J.W. Choi, H.S. Jun, S. Cho, Silver nanoflower-reduced graphene oxide composite based micro-disk electrode for insulin detection in serum, Biosens. Bioelectron. 80 (2016) 307–314.
[35] T.X. Wei, W.W. Tu, B. Zhao, Y.Q. Lan, J.C. Bao, Z.H. Dai, Electrochemical monitoring of an important biomarker and target protein: VEGFR2 in cell lysates, Sci. Rep. UK 4 (2014).
[36] A.J. Bard, L.R. Faulkner, Electrochemical Methods : Fundamentals and Applications, 2nd ed. John Wiley, New York, 2000.
[37] C.K. Dixit, S.K. Vashist, F.T. O'Neill, B. O'Reilly, B.D. MacCraith, R. O'Kennedy, Development of a high sensitivity rapid Sandwich ELISA procedure and its comparison with the conventional approach, Anal. Chem. 82 (2010) 7049–7052.
[38] T. Noyhouzer, I. Valdinger, D. Mandler, Enhanced Potentiometry by metallic nanoparticles, Anal. Chem. 85 (2013) 8347–8353.
[39] M. Tatarkovic, G. Broncova, M. Krondak, Electrochemical impedance spectroscopy and its application in chemical analysis, Chem. List. 106 (2012) 1067–1074.
[40] Y.Y. Niu, J. Liu, W. Chen, C.X. Yin, W.J. Weng, X.Y. Li, X.L. Wang, G.J. Li, W. Sun, A direct electron transfer biosensor based on a horseradish peroxidase and gold nanotriangle modified electrode and electrocatalysis, Anal Methods UK 10 (2018) 5297–5304.
[41] S.Y. Tan, R.A. Lazenby, K. Bano, J. Zhang, A.M. Bond, J.V. Macpherson, P.R. Unwin, Comparison of fast electron transfer kinetics at platinum, gold, glassy carbon and diamond electrodes using Fourier-transformed AC voltammetry and scanning electrochemical microscopy, Phys. Chem. Chem. Phys. 19 (2017) 8726–8734.
[42] Y.Y. Zhang, S. Xu, X.Q. Xiao, Y. Liu, Y.Y. Qian, Y.X. Li, Single gold nanowire electrodes and single Pt@au nanowire electrodes: electrochemistry and applications, Chem. Commun. 53 (2017) 2850–2853.
[43] D.R. Cantrell, S. Inayat, A. Taflove, R.S. Ruoff, J.B. Troy, Incorporation of the electrode-electrolyte interface into finite-element models of metal microelectrodes, J. Neural Eng. 5 (2008) 54–67.
[44] C. Gabrielli, M. Keddam, N. Portail, P. Rousseau, H. Takenouti, V. Vivier, Electrochemical impedance spectroscopy investigations of a microelectrode behavior in a thin-layer cell: experimental and theoretical studies, J. Phys. Chem. B 110 (2006) 20478–20485.
[45] S.K. Arya, G. Chornokur, M. Venugopal, S. Bhansali, Dithiobis(succinimidyl propionate) modified gold microarray electrode based electrochemical immunosensor for ultrasensitive detection of cortisol, Biosens. Bioelectron. 25 (2010) 2296–2301.
[46] A.K. Yagati, J. Min, S. Cho, Electrosynthesis of ERGO-NP Nanocomposite films for Bioelectrocatalysis of horseradish peroxidase towards H_2O_2, J. Electrochem. Soc. 161 (2014) G133–G140.
[47] M. Javid, G. Callender, C. Quinn, T. Carling, P. Donovan, R. Udelsman, Primary hyperparathyroidism with normal baseline intraoperative parathyroid hormone: a challenging population, Surgery 161 (2017) 493–498.
[48] X.X. Li, L.H. Shen, D.D. Zhang, H.L. Qi, Q. Gao, F. Ma, C.X. Zhang, Electrochemical impedance spectroscopy for study of aptamer-thrombin interfacial interactions, Biosens. Bioelectron. 23 (2008) 1624–1630.
[49] Y. Huang, M.C. Bell, I.I. Suni, Impedance biosensor for Peanut protein Ara h 1, Anal. Chem. 80 (2008) 9157–9161.
[50] H.M. Ozcan, M.K. Sezginturk, Detection of parathyroid hormone using an electrochemical impedance biosensor based on PAMAM Dendrimers, Biotechnol. Prog. 31 (2015) 815–822.
[51] H.M. Ozcan, K. Yildiz, C. Cakar, T. Aydin, E. Asav, A. Sagiroglu, M. Sezginturk, Ultrasensitive Impedimetric biosensor fabricated by a new immobilisation technique for parathyroid hormone, Appl. Biochem. Biotech. 176 (2015) 1251–1262.
[52] C.S. Simsek, M.N.S. Karaboga, M.K. Sezginturk, A new immobilization procedure for development of an electrochemical immunosensor for parathyroid hormone detection based on gold electrodes modified with 6-mercaptohexanol and silane, Talanta 144 (2015) 210–218.
[53] H.U. Kim, H.Y. Kim, A. Kulkarni, C.S. Ahn, Y.H. Jin, Y. Kim, K.N. Lee, M.H. Lee, T. Kim, A sensitive electrochemical sensor for in vitro detection of parathyroid hormone based on a MoS2-graphene composite, Sci. Rep. UK 6 (2016).
[54] H.Y. Kim, S. Sato, S. Takenaka, M.H. Lee, Membrane-based microwave-mediated electrochemical immunoassay for the In vitro, highly sensitive detection of osteoporosis-related biomarkers, Sensors-Basel 18 (2018).
[55] A. Chamorro-Garcia, A. de la Escosura-Muniz, M. Espinoza-Castaneda, C.J. Rodriguez-Hernandez, C. de Torres, A. Merkoci, Detection of parathyroid hormone-like hormone in cancer cell cultures by gold nanoparticle-based lateral flow immunoassays, Nanomed-Nanotechnol 12 (2016) 53–61.
[56] W.U. Dittmer, P. de Kievit, M.W.J. Prins, J.L.M. Vissers, M.E.C. Mersch, M.F.W.C. Martens, Sensitive and rapid immunoassay for parathyroid hormone using magnetic particle labels and magnetic actuation, J. Immunol. Methods 338 (2008) 40–46.
[57] O.S. Kwon, S.R. Ahn, S.J. Park, H.S. Song, S.H. Lee, J.S. Lee, J.Y. Hong, J.S. Lee, S.A. You, H. Yoon, T.H. Park, J. Jang, Ultrasensitive and selective recognition of peptide hormone using close-packed arrays of hPTHR-conjugated polymer nanoparticles, ACS Nano 6 (2012) 5549–5558.